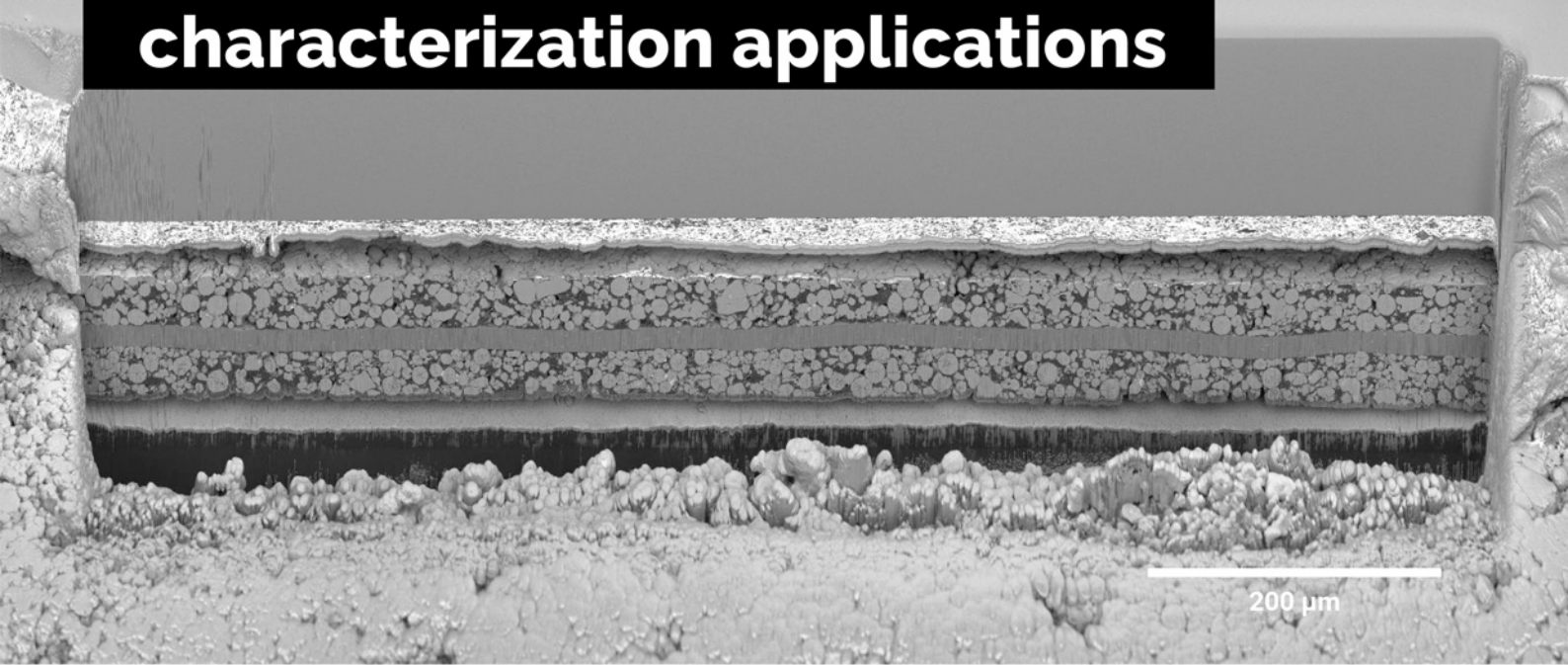


# A unique combination of Plasma FIB and field-free UHR SEM for the widest range of multiscale materials characterization applications



1 mm cross-section through a Li-ion battery electrode

## TESCAN AMBER X

- ✓ High throughput, large area FIB milling up to 1 mm
- ✓ Ga-free microsample preparation
- ✓ Ultra-high resolution, field-free FE-SEM imaging and analysis
- ✓ In-column SE and BSE detection
- ✓ Spot optimization for high-throughput, multi-modal FIB-SEM tomography
- ✓ Superior field of view for easy navigation
- ✓ Essence™ easy-to-use, modular graphical user interface



For more information visit

[www.tescan.com](http://www.tescan.com)

# Enhanced Output of On-Body Direct-Current Power Textiles by Efficient Energy Management for Sustainable Working of Mobile Electronics

Renwei Cheng, Chuan Ning, Pengfei Chen, Feifan Sheng, Chuanhui Wei, Yihan Zhang, Xiao Peng, Kai Dong,\* and Zhong Lin Wang\*

Triboelectric power textile (TPT) that can harvest widespread but always neglected human biomechanical energy is considered a promising and reliable energy source for wearable electronics. However, the alternating current and high impedance of triboelectric nanogenerators as well as the meager electrical output caused by the properties of the textile itself greatly restrict its practical applications. Here, an autonomous power textile with practical application value, which consists of a high-output direct-current TPT (DC-TPT) and a miniaturized energy management module (EMM), is achieved for continuous operation of wearable and mobile electronics. The home-preparable multiarray DC-TPT can harvest transferred charge of 5.5  $\mu\text{C}$  per cycle with nine repeating units. Moreover, it is found that incorrect sewing positions of the polytetrafluoroethylene (PTFE) yarn change the working mechanism with a decreased DC output. The EMM with energy conversion efficiency of 82.6% can reduce the impedance of DC-TPT from 200 to 1.6  $\text{M}\Omega$ . With its powerful assistance, the watch can work continuously for 172 s just by manually sliding the DC-TPT 1.6 s on an arm, and wireless signals can be transmitted to 281 m away after sliding for 2 min. Various widely used electronics can also be easily and continuously driven.

the first choice, the limited lifetime and toxic chemicals may restrict their future applications in distributed device systems under the demand of sustainable and environment-friendly energy sources.<sup>[9–12]</sup> Fortunately, our body and surrounding environment, including biomechanical energy, body heat, and sunshine, are rich of renewable energy. As for environmental energy harvesters, the promising solar cells and thermoelectric generators have strict requirements on the intensity of sunlight and the level of thermal gradient, respectively. For human who often stay indoors with suitable temperatures, these may seriously affect their performance as on-body energy harvester.<sup>[13,14]</sup> As for biomechanical energy harvesters, triboelectric nanogenerator (TENG), which originated from Maxwell's displacement current,<sup>[15–18]</sup> is more conducive to harvesting low frequency human motion than traditional electromagnetic

generators and exhibits higher electrical output than piezoelectric nanogenerators.<sup>[19,20]</sup>

In the nearly three hundred years of the amazing development of science and technology, the clothes that have accompanied us for thousands of years have trapped at the functions of warmth and beauty for long time. As an ideal platform for on-body devices with compelling features of wearing comfort, light weight, high flexibility, and indispensability, developing smart textiles with more functions are urgent and meaningful.<sup>[21–24]</sup> The combination of textiles and TENG is naturally considered

## 1. Introduction

The rapidly developed wearable electronics in the context of the era of Internet of Things, including sensing and physiological monitoring,<sup>[1,2]</sup> data communication,<sup>[3,4]</sup> display,<sup>[5,6]</sup> human–machine interfaces,<sup>[7,8]</sup> etc., enriches and transforms the quality of our lives. However, these electronics cannot survive after leaving the source of their life–energy, no matter how smart or vital they are. Although the currently widely used portable batteries or supercapacitors seem intuitively to be

R. Cheng, C. Ning, P. Chen, F. Sheng, C. Wei, Y. Zhang, X. Peng, K. Dong, Z. L. Wang  
CAS Center for Excellence in Nanoscience  
Beijing Key Laboratory of Micro-Nano Energy and Sensor  
Beijing Institute of Nanoenergy and Nanosystems  
Chinese Academy of Sciences  
Beijing 101400, China  
E-mail: dongkai@binn.cas.cn; zlwang@binn.cas.cn

 The ORCID identification number(s) for the author(s) of this article can be found under <https://doi.org/10.1002/aenm.202201532>.

R. Cheng, C. Ning, P. Chen, C. Wei, Y. Zhang, X. Peng, K. Dong, Z. L. Wang  
School of Nanoscience and Technology  
University of Chinese Academy of Sciences  
Beijing 100049, China

F. Sheng  
School of Chemistry and Chemical Engineering  
Center on Nanoenergy Research  
Guangxi University  
Nanning 530004, China

Z. L. Wang  
School of Material Science and Engineering  
Georgia Institute of Technology  
Atlanta, GA 30332, USA

DOI: 10.1002/aenm.202201532

to be an important solution for the energy sources of wearable electronics.<sup>[25–29]</sup>

However, the bottlenecks of limited and alternating current (AC) pulsed electrical output hindered the progress of TENG in the translation of Lab-to-Fab. The AC output of the traditional TENG based on the coupling effect of triboelectrification and electrostatic induction cannot directly meet the direct current (DC) demand of most electronic devices.<sup>[30–33]</sup> In general, there are two ways to convert AC to DC, including adding rectifiers (electronic bridge rectifier<sup>[34,35]</sup> and mechanical rectifier<sup>[36,37]</sup>) and varying the physical effects (tribovoltaic effect<sup>[38,39]</sup> and dielectric breakdown effect<sup>[26,40]</sup>). Undeniably, as the most widely used method, it is very convenient to directly select a low-cost commercial electronic rectifier bridge. Nevertheless, the rigid electronic rectifier bridge with nearly 10% power consumption is unfriendly to wearable textile-based TENG (T-TENG).<sup>[26]</sup> The mechanical rectifier bridge, which usually requires the two electrodes of the TENG and the two electrodes of the external circuit to be connected alternately and regularly, may be incompatible with the flexible T-TENG.<sup>[36,37]</sup> The voltage output of the TENG based on the tribovoltaic effect limited by the low built-in electric field is usually lower than 10 V, while the current is not improved.<sup>[39]</sup> TENG based on dielectric breakdown effect has been extensively studied in the past three years due to its high output characteristics, but researchers have almost focused on hard TENG that not suitable for wearable electronics.<sup>[41–44]</sup> In addition, the extreme mismatch between capacitive TENG with high internal resistance ( $\approx 100\text{ M}\Omega$  to  $\approx 1\text{ G}\Omega$ ) and electronic devices with low internal resistance ( $\approx 1\ \Omega$  to  $\approx 10\text{ k}\Omega$ ) results in low available energy for directly powering electronic devices.<sup>[45,46]</sup> Various energy management strategies focusing on reducing voltage and increasing current, including transformer, LC buck convertor, and switched capacitors, have been proposed to further improve the electrical output of TENG. Magnetic and bulky transformers may not be suitable for integration on clothes.<sup>[47,48]</sup> As for switched capacitors, more capacitors and diodes are required to obtain better results, which is also not conducive to miniaturization on clothes.<sup>[49,50]</sup> The miniaturized buck circuit with a few electronic components may be beneficial to integrate on textiles. A suitable switch is the key to obtain an effective energy management module (EMM) based on buck circuit. Mechanical switches,<sup>[51]</sup> dielectric breakdown switches<sup>[52]</sup> and electronic switches<sup>[53,54]</sup> have been successfully used in buck circuits. Electronic switches are favored due to their small size, automation, and cheap price. However, active electronic switches, such as metal-oxide-semiconductor field-effect transistor, require an external power sources. Although it can be provided by TENG itself, TENG still suffers from avoidable energy losses.<sup>[53]</sup> Therefore, passive electronic switches should be considered for the energy management strategy of T-TENG.

Herein, a home-preparable and high-output DC triboelectric power textile (DC-TPT) and a miniaturized but efficient EMM are developed to continuously drive wearable and mobile electronics. DC-TPT, which consists of a textile substrate, friction electrode (generating charges), breakdown electrode (harvesting charges), and polytetrafluoroethylene (PTFE) yarn (maintaining a stable and tiny breakdown gap), can be sewn or prepared directly on our clothes to harvest biomechanical energy with

high output. The electrical output increases with the increasing of the number of repeating units ( $N$ ), and the transferred charge reaches  $5.5\ \mu\text{C}$  per cycle when  $N = 9$ . The size of the breakdown electrode and the friction electrode as well as the sewing position of the PTFE yarn are systematically explored. In particular, the DC electrical output of the TPT without PTFE yarn is also thoroughly studied. Furthermore, a coin-sized EMM with a conversion efficiency of 82.6% can be worn on our clothes and combined with the high-output DC-TPT to form an autonomous power textile. The matched resistance is reduced from  $200\text{ M}\Omega$  to  $1.6\text{ M}\Omega$ , which endows a 2117 times improvement in charging energy storage devices. As a wearable self-powered system, a watch can continuously work 172 s after sliding the DC-TPT for only 1.6 s. The signal of the portable sensor can be wirelessly transmitted to the computer receiver 281 m away. Moreover, four 30 W dish bulbs can be lit up and the words on the paper can be clearly illuminated when the EMM is in pulse output mode. Therefore, our DC-TPT exhibits broad application potential for sustainable working of mobile electronics.

## 2. Results and Discussion

### 2.1. Application Scenarios and Structure of the DC-TPT

We need “infinite-lifetime” and “environment-independent” energy harvesters outdoors to power the electronics or charge the batteries when the carried energy sources are depleted, which may even save our lives in some emergency scenarios. The development of various energy harvesting technologies today provides us with a variety of options. They have their own advantages and disadvantages (Table S1, Supporting Information), but the mutual cooperation and complementation between them may offer us better services. For example, the lack of sun and the need to keep warm may limit the applications of solar cells and thermoelectric generators for people exploring in the forest. The bulkiness and demand for high frequency motion of traditional electromagnetic generators with high mass density ferromagnetic materials may conflict with portability. The TPT we proposed in this paper may fill the insufficiency of these great energy harvesting technologies. As demonstrated in **Figure 1a**, our autonomous power textile consists of the DC-TPT, EMM, and triboelectric layer. The DC-TPT can be directly prepared on our clothes to harvest biomechanical energy, drive wireless transmitters to communicate with others, light up the bulbs on our heads to illuminate the way in the dark, also power some small emergency electronics in our backpacks. It can provide us with emergency electrical energy, whether it is day or night, in high or low temperature environment.

Different from rigid substrates, the daily wearable textile seems to be born for wearable electronics, but it also brings some challenges to structural design that needs to be shaped. We consider that coplanar-electrode is more conducive to the multiarray high-output DC power textile based on the triboelectrification and air breakdown without affecting the wearable characteristics of textile. To create the stable and tiny air gap between the soft textile and the triboelectric layer on an all-textile device, polytetrafluoroethylene (PTFE) yarn is

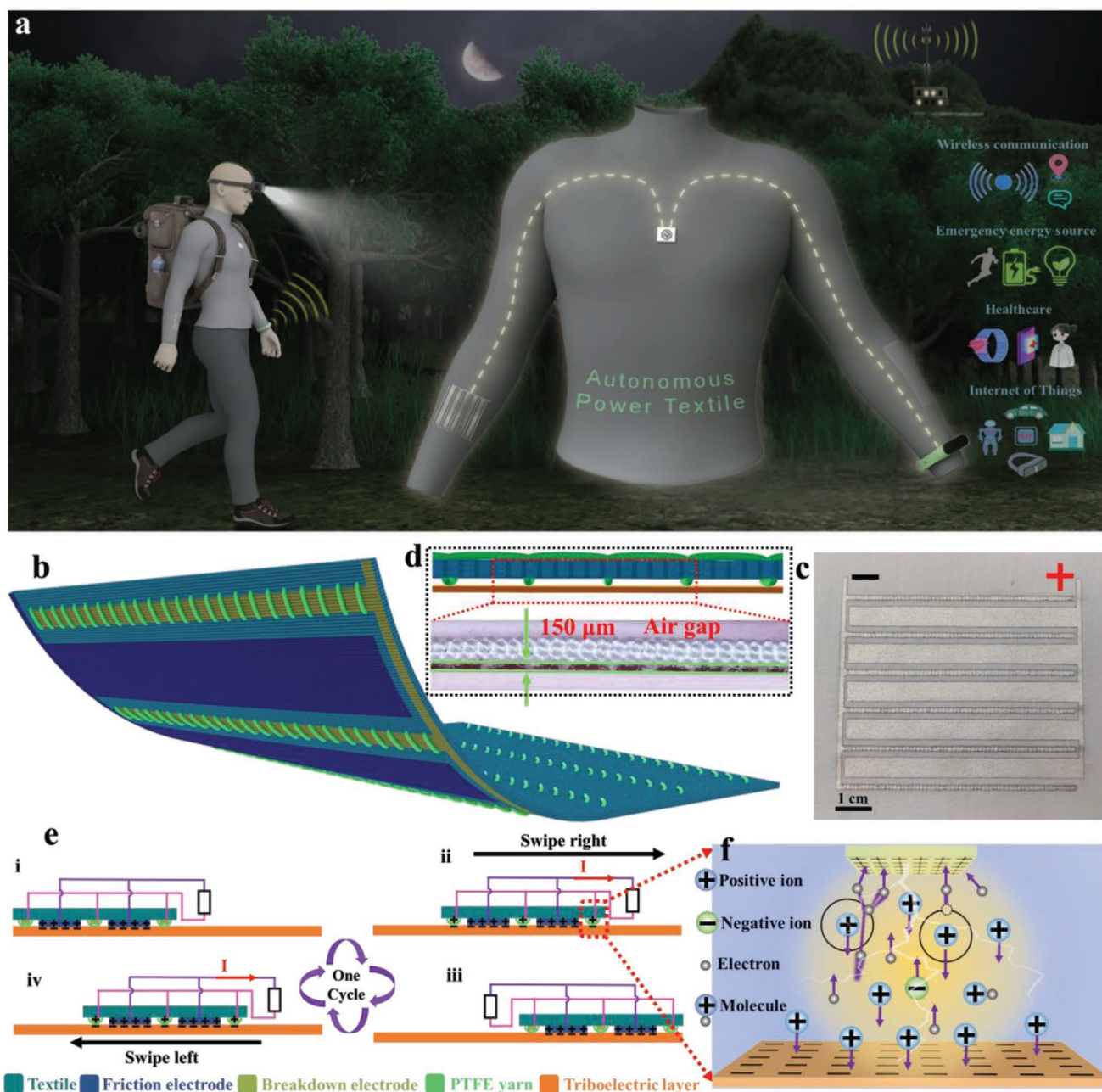


**Figure 1.** Application scenarios, structures, and working mechanism of the DC-TPT. a) Application scenarios and compositions of energy harvesting clothes. b) Schematic illustration and c) the actual photograph of the DC-TPT. d) The stable and tiny air breakdown gap. e) The working mechanism of the DC-TPT. f) Corona discharge in air gap of the DC-TPT.

deliberately selected and sewn on the breakdown electrode due to its outstanding resistance to abrasion (Figure 1b). The bottom and top schematic diagrams are shown in Figure S1 (Supporting Information). The entire DC-TPT only consists of textile substrate (polyester–cotton fabric), two kinds of electrodes (breakdown electrode and friction electrode), and PTFE yarn, which is easy to achieve, requires no high-end equipment, and is home-prepared. The friction electrode and breakdown electrode are neatly prepared on the textile, and serve as positive and negative when the electron-friendly materials as triboelectric layers, respectively (Figure 1c). Moreover, the DC-TPT

can be prepared directly onto our clothing (Figure S2, Supporting Information). The breakdown electrode is regularly surrounded by PTFE yarn (Figure S3a, Supporting Information). The stable and tiny air gap (150 μm), which is equivalent to the diameter of the PTFE yarns, is successfully realized by the support of PTFE yarn (Figure 1d). It is noteworthy that the size of the air gap can be easily controlled by varying the diameter of the PTFE yarns without complicated experiments. The friction electrode, breakdown electrode and fine PTFE yarn act as charge generator, charge harvester and spacer, respectively. Owing to the excellent conductivity and strong tendency to lose

electrons of silver paste, it is selected and brushed on the textile substrate as the electrodes. The conductivity of the electrodes is displayed in Figure S4a,b (Supporting Information). There is no obvious variation in conductivity and mass even after sliding on the fluorinated ethylene propylene (FEP) film for 6 h (Figure S5, Supporting Information), indicating the strong adhesion between silver paste and textile. Moreover, the naturally high flexibility (Figure S4b, Supporting Information), good breathability (Figure S6, Supporting Information), outstanding moisture permeability ( $8492 \text{ g m}^{-2} \text{ day}^{-1}$ ,  $38 \text{ }^\circ\text{C}$ ,  $90\% \text{ RH}$ ), and light weight ( $16.5 \text{ mg cm}^{-2}$ , Figure S4c, Supporting Information) endows the DC-TPT excellent wearability.

Unlike traditional AC-TENG, DC-TPT directly outputs DC based on the coupling effect of triboelectrification and electrostatic breakdown. FEP film with high fluorine content is selected as the triboelectric layer to obtain a higher surface charge density and further break down the air between the breakdown electrode and FEP film to create a conductive plasma channel. For the triboelectrification, the overlap of the electron cloud of the silver atoms in the friction electrode and fluorine atoms in the FEP film will result in electrons transfer from the silver atoms to fluorine atoms when the DC-TPT slides on the FEP film. Electrons will be retained at the surface state energy level of the FEP film due to the potential barrier between the two atoms as they are separated.<sup>[55,56]</sup> Therefore, friction electrode are positively charged with an equal number of negative charges generated on the surface of the FEP film. For the air breakdown process, the high surface charge density of the FEP film not covered by the friction electrode will not be neutralized when the DC-TPT slides, which will result in a strong electric field between the FEP film and the breakdown electrode (Figure S7, Supporting Information). The air between them will be easily broken down with the stable and tiny air gap (the critical breakdown electric field of air is  $\approx 3 \text{ kV mm}^{-1}$  according to Paschen's law). There will be a conductive plasma channel between breakdown electrode and FEP film when air breakdown occurs (it is usually corona discharge, Figure 1f). The details of corona discharge in the breakdown gap can be found in Note S1 (Supporting Information). Driven by the high potential difference, the positive charges on the friction electrode will neutralize the negative charges on the surface of the FEP film through the external circuit and plasma channel. Thus, there will be a unidirectional current in the external circuit as DC-TPT slides on the FEP film (Figure 1e). The obvious decrease in the surface potential of the FEP film after air breakdown further proves the above mechanism (Figure S8, Supporting Information). A set of typical electrical output of the DC-TPT is shown in Figure S9 (Supporting Information). The unidirectional current, charge transfer per cycle and voltage reach  $6.52 \text{ } \mu\text{A}$ ,  $2.97 \text{ } \mu\text{C}$ , and  $1229 \text{ V}$ , respectively (the number of repeating units  $N$  is 5). Since the substrate does not play an important role in the triboelectrification and air breakdown, the substrate can be replaced with various types of textiles without affecting electrical output (Figure S10, Supporting Information).

## 2.2. Electrical Output Performance of the Single-Unit DC-TPT

To fully understand the DC-TPT, we first systematically investigate the influence of various structural parameters

(summarized in Table S2, Supporting Information) of single-unit DC-TPT on the electrical output (Figure 2a). Generally, the impact of the breakdown electrode, the friction electrode, and the PTFE yarn will be focused on. The number of generated charges will be determined by the friction electrode, while the breakdown electrode and the PTFE yarn will affect the number of harvested charges. A linear motor is utilized to drive DC-TPT for reciprocating motion. We first pay attention to the breakdown electrode. The  $A$  shows no obvious relationship with the electrical output, which indicates that the width of the breakdown electrode has little effect on the charge harvesting ability (Figure S11, Supporting Information). However, the longer breakdown electrode will increase the charge harvesting area when  $B$  is less than  $D$ , and the output increases with an increase in  $B$  (Figure S12, Supporting Information). Considering the miniaturization of the DC-TPT,  $A = 1 \text{ mm}$  is selected in the following experiments, but the value of  $B$  will be chosen according to the actual needs considering the contradiction between output and miniaturization. The output decreases with the increase of the values of  $C$  and  $D$ , which may be attributed to the insufficient contact state with the decrease of pressure under the same weight of  $1.5 \text{ kg}$  (Figure S13, Supporting Information). Separately increasing the value of  $B$  or  $D$  will lead to the opposite results, while the output will increase with the increasing of  $B$  and  $D$  ( $B = D$ ), indicating that the charge harvesting area shows a greater impact on the output than the pressure (Figure 2e). Wear-resistant and fine PTFE yarn will successfully lift up the breakdown electrode, and the length of the air gap is determined by the diameter of the PTFE yarn ( $d_{\text{PTFE}}$ ). Therefore, air gaps with different lengths can be easily obtained by varying  $d_{\text{PTFE}}$ . Note that the area of the breakdown electrode covered by the PTFE yarn will hardly be broken down owing to the ultrahigh breakdown field strength of the solid dielectric material ( $>1 \text{ MVcm}^{-1}$ ). Therefore, the DC-TPTs with different  $d_{\text{PTFE}}$  have different values of  $H$  to control the same effective length of the breakdown electrode (the effective length is the total length of the breakdown electrode that is not covered by PTFE yarns). The electrical output decreases with the increase of the values of  $E$  (Figure 2b–d). According to Paschen's law, the best distance for air breakdown is about a few microns, and the length of air gap in our experiment exceeds this value.<sup>[57]</sup> Therefore, the difficulty of breakdown will gradually increases as the length of the air gap increases, which will further leads to low electrical output. To obtain a higher output, the PTFE yarn with  $d_{\text{PTFE}} = 0.15 \text{ mm}$  will be chosen in the following experiments. The PTFE yarn is sewn next to the edge of the breakdown electrode. With the value of  $F$  increases, the electrical output increases first, and then maintains a constant value (Figure 2f). Similar results appear for DC-TPT with  $d_{\text{PTFE}} = 0.3 \text{ mm}$  (Figure S14, Supporting Information). The DC-TPT with  $F = 0.5 \text{ mm}$  is elaborately observed ( $d_{\text{PTFE}} = 0.3 \text{ mm}$ ). It is found that the PTFE yarn may also prop up the edge of friction electrode while suspending the breakdown electrode when the  $F$  is small (Figure S15, Supporting Information). In this case, some of the electrons on the surface of the FEP may directly neutralize the positive charges on the friction electrode through the conductive plasma channel

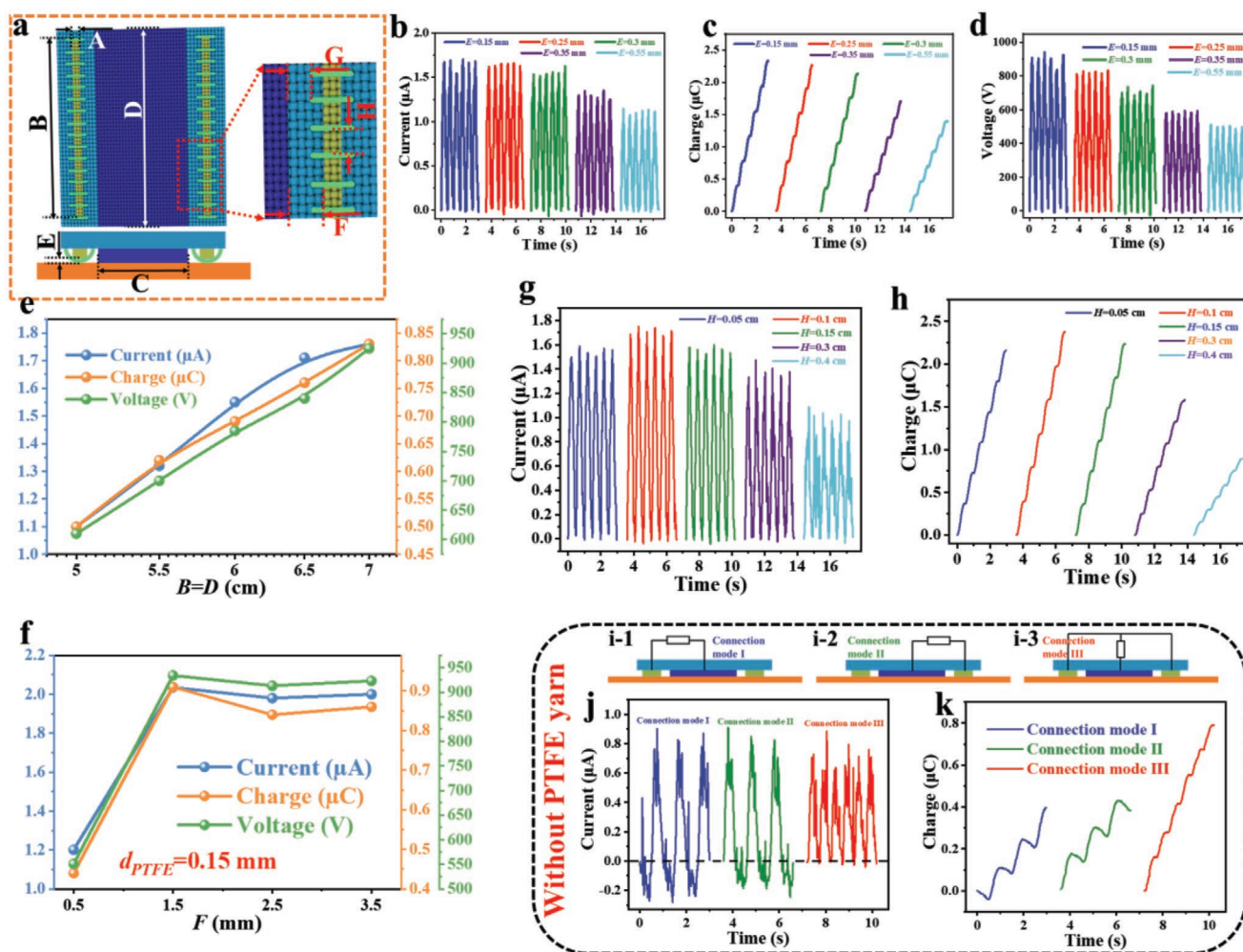


**Figure 2.** Electrical output performance of the DC-TPT with single unit. a) Various structural parameters under investigation. b) The current, c) charge transfer, and d) voltage of the DC-TPT with different air gap. Variation of the output performance of the DC-TPT with e) different  $B$  and  $D$  values, and f)  $F$  values. g) The current and h) charge transfer of the DC-TPT with different  $H$  values. i) Different connection mode of the power fabric without PTFE yarn. j, k) The electric output performance of the power fabric without PTFE yarn in different connection modes.

between them, instead of the external circuit, which is unfavorable for the electrical output. Moreover, by varying the distance between the PTFE yarn and the friction electrode (defined as  $G$ ), the electrical output decreases when the value of  $G$  is very small, which further verifies this explanation (Figure S16, Supporting Information).

Next, we focus on discussing the parameter  $H$ . With the increase of  $H$ , the electrical output first increases and then decreases, the maximum value can be obtained when  $H = 1$  mm (Figure 2g,h). The decrease of  $H$  will create a denser covering of breakdown electrode by PTFE yarn, resulting in the reduction of the effective length of the breakdown electrode and lower output. However, the friction electrode will be in contact with the FEP film when  $H$  increases, and the working mode in Figure 1e will be invalid (Figure S17, Supporting Information). The triboelectric power textile without PTFE yarn (named WP-TPT) is prepared to investigate the situation when the breakdown electrode is in contact with the triboelectric layer. Our DC-TPT output DC in three different connection modes, and the output of connection mode 3 is the sum of that of con-

nection modes 1 and 2 (Figure S18, Supporting Information). The WP-TPTs with similar connection modes are shown in Figure 2i. Note that WP-TPT initially slides from right to left in these three connection modes. Different from the DC-TPT, WP-TPT outputs AC in connection modes 1 and 2, DC in connection mode 3 (Figure 2j,k). Additionally, the output of DC-TPT is higher than that of WP-TPT under the same experimental conditions (connection mode 3). The two electrodes TPT without PTFE yarn (TE-TPT) is designed to investigate the origin of these phenomena (Figure S19, Supporting Information). The output and the corresponding sliding state are shown in Figure S20a–c (Supporting Information). It can be found that the current flows from the front electrode to the back electrode in the sliding direction (Figure S20d,e, Supporting Information). When the electrode slides on the FEP film, as the number of sliding times increases, the total number of transferred charges will gradually increases until saturation, while the number of transferred charges of single half sliding cycle will gradually decreases (Figure S21, Note S2, Supporting Information).<sup>[58,59]</sup> Therefore, when the TE-TPT slides from left to

right, the charges in Figure S22 (Supporting Information) will satisfy the following formula

$$(Q_1 + Q_3) > (Q_2 + Q_4) \quad (1)$$

where  $Q_1$ ,  $Q_2$ ,  $Q_3$ , and  $Q_4$  are the charges in the area of the FEP film corresponding to the electrode-R, the area of the FEP film corresponding to the electrode-L, electrode-R, and the electrode-L, respectively. Detailed derivation is displayed in Note S3 (Supporting Information). The results will be the opposite when the sliding direction is changed. Therefore, driven by electrostatic induction and the difference in charge density, the current will move in the direction from electrode-R to the electrode-L after connecting them with a wire (Figure S22c, Supporting Information). Air breakdown will occur when the potential difference between electrode-L and FEP film in the region A (the area not covered by electrodes) exceeds the critical value (Figures S22c and S23, Supporting Information). The neutralization of the charges caused by air breakdown will reduce the surface charge density of the FEP film in the region A, thus the triboelectrification in the next cycle can be repeated. The surface potential of the FEP film after the TE-TPT slides left and right repeatedly further verifies the above explanation (Figure S24, Supporting Information). The summary of the working mechanism of TE-TPT is shown in Figure S25 and Note S4 (Supporting Information). Furthermore, by varying the width of electrode-R (defined as  $X$ ), it is clear that both the output current ( $I_B$ ) and transfer charge ( $Q_B$ ) decrease with the decreasing of the  $X$  value

when sliding the TE-TPT from left to the right (Figure S26, Supporting Information). As we know,

$$Q_B = \frac{(Q_1 + Q_3) - (Q_2 + Q_4)}{2} \quad (2)$$

$$I_B = \frac{\Delta Q_B}{\Delta t} = \frac{\Delta[(Q_1 + Q_3) - (Q_2 + Q_4)]}{2\Delta t} \quad (3)$$

where  $Q_B > 0$  according to formula (1), the  $\Delta Q_B$  is the number of transferred charges in tiny time  $\Delta t$ . Decreased  $X$  will result in a decreased  $(Q_1 + Q_3)$ , which in turn reduces  $Q_B$  and  $I_B$ . However, when the TE-TPT slides from right to the left, the  $I_A$  and  $Q_A$  are invariant at different  $X$  may be attributed to the tiny  $(Q_1 + Q_3)$ . These may also explain the alternating current and the unequal electrical output when WP-TPT slides left and right in connection modes 1 and 2 in Figure 2j,k. It is worth noting that the output of the connection mode 3 is the sum of that of mode 1 and mode 2, while the current direction of mode 1 and mode 2 is opposite, which may result in the lower output of the WP-TPT (without PTFE yarn) than the DC-TPT (with PTFE yarn).

### 2.3. Electrical Output Performance of the Multiunit DC-TPT

The output of the DC-TPT can be further improved by increasing the number of the repeating units  $N$  (Figure 3a and

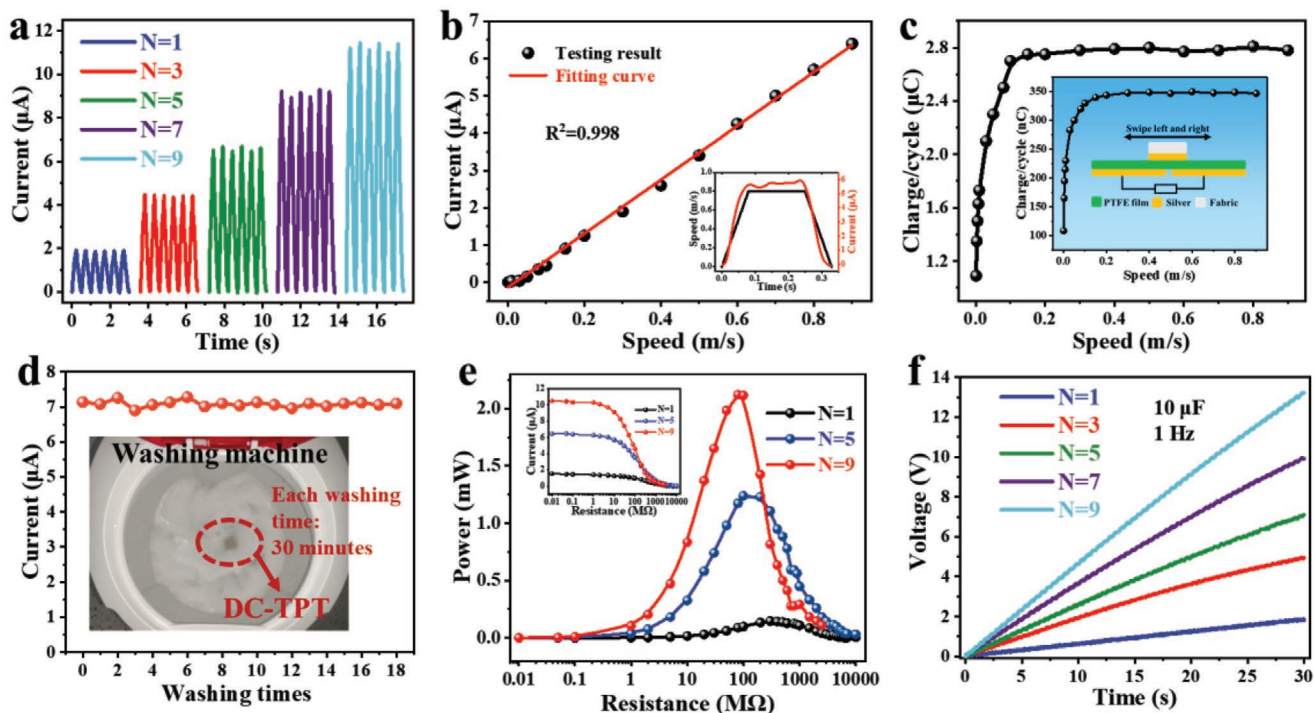


**Figure 3.** Electric output performance of the DC-TPT with multiple units. The influence of the number of units ( $N$ ) on the output current of DC-TPT (The number of friction electrodes and breakdown electrodes are  $N$  and  $N+1$ , respectively). b) Variation of the current and c) charge transfer of the DC-TPT under different sliding speed ( $N = 5$ ). The inset in (b) is the electrical output at  $0.8 \text{ m s}^{-1}$ . The illustration in (c) is the charge transfer of the freestanding mode TENG under different sliding speed. d) The washability test of the DC-TPT ( $N = 5$ ). e) The power of the DC-TPT with different  $N$  values. The inset shows the corresponding current. f) Variations of the voltage of  $10 \mu\text{F}$  electrolytic capacitor with different  $N$  values.

Figure S27, Supporting Information). The transferred charge can reach  $5.5 \mu\text{C}$  in one cycle when  $N = 9$  (the sliding distance  $J$  is 20 cm,  $A = H = 1 \text{ mm}$ ,  $F = 1.5 \text{ mm}$ ,  $C = 5 \text{ mm}$ ,  $B = D = 6 \text{ cm}$ ). Considering the surface charge density of the triboelectric layer will determine the electrical output of the DC-TPT (Figure 1e), three kinds of triboelectric layers have been investigated, including FEP and PTFE with strong electronic capabilities as well as nylon with strong electronic loss ability. Benefit from higher fluorine content, FEP exhibits better electrical output than the PTFE, while the current of positively charged nylon is opposite to negatively charged FEP and PTFE (Figure S28, Supporting Information). As the mass of the weight applied onto the DC-TPT increases, the electrical output gradually increases until reaches a stable value, which may be attributed to the variation of the effective contact area ( $N = 3$ , Figure S29, Supporting Information).<sup>[15]</sup> As a wearable energy harvester for human motion energy, sliding speed, sliding distance (defined as  $J$ ), acceleration and deceleration may have a significant impact on the electrical output. A constant current can be obtained when the DC-TPT slides at a constant speed (the inset of Figure 3b). The current nearly increase with sliding speed linearly, which may be attributed to the accelerated charge transfer speed (Figure 3b). Regarding the transferred charge, we found that it is not independent of speed as previously reported in the literature,<sup>[40]</sup> which is usually considered to be attributed to the unchanged sliding area. The transferred charge will increase with the increase of speed when it is lower than  $0.1 \text{ m s}^{-1}$ . The freestanding mode TENG is utilized as a probe to characterize the variation of surface charge on the FEP film under different sliding speeds (inset of Figure 3c). Note that the two electrodes are deliberately enlarged to ensure the upper slider moves at a constant speed when it reaches their demarcation. More friction times will result in a higher surface charge density before it is saturated.<sup>[58]</sup> Therefore, the test is carried out from high speed to low speed to avoid its impact on the surface charge density at high speed. It is clear that both the trend and percentage of the surface charge of the freestanding mode TENG at different sliding speeds are similar to those of the harvested charge of the DC-TPT (Figure 3c). It indicates that the variation of the harvested charge of the DC-TPT with the sliding speed may results from the change of the surface charge density of the FEP film. Different generated and dissipated charges can cause changes in surface charge density. For contact-separated mode TENG, there may be little difference in the number of generated charge at different frequencies due to the short contact time. As shown in Figure S30 (Supporting Information), the number of transferred charge only decreases by 11.3% when the frequency is reduced from 2.5 to 0.01 Hz, which is more likely due to the charge dissipation. The low-speed dissipation of charges on the surface of the FEP film does not seem to be responsible for the variation of surface charge density of sliding-mode TENG (DC-TPT and free-standing mode TENG) at different speeds. Therefore, the reduction of the generated charge may be the main reason for the decrease of the harvested charge at low speed, which may be further resulted from the gentle contact between the silver electrode and the FEP film under low speed. Keeping the distance constant ( $J = 20 \text{ cm}$ ) and change the acceleration and deceleration (the values of acceleration and deceleration keep the same and are 1.568, 3.2, 5.408,

8.192, 11.552  $\text{m s}^{-2}$ , respectively) to obtain different sliding frequencies (0.7, 1, 1.3, 1.6, 1.9 Hz). As shown in Figure S31 (Supporting Information), the time related current can be scaled up with the increase of the sliding frequency, while the invariant transferred charge may be due to the constant sliding distance and high sliding speed (all of them exceed  $0.1 \text{ m s}^{-1}$ ). Similarly, both the current and the transferred charge will increase with the increase of the sliding distance ( $J$ ) when the acceleration and deceleration are maintained at  $2.72 \text{ m s}^{-2}$  (Figure S32, Supporting Information). Moreover, DC-TPT is more suitable for low humidity environment owing to the negative impact of high humidity on surface charge density of the FEP film (Figure S33, Supporting Information).<sup>[26]</sup>

As a textile-based wearable energy harvester, our DC-TPT also exhibits excellent washing resistance. Even after stirring in a commercial washing machine with laundry detergent for 9 h, the electrical output shows no significant drop due to the strong adsorption between the silver paste and the fabric (Figure 3d). Moreover, DC-TPT also displays an outstanding potential for long-term daily use during one month of intermittent loading (Figure S34, Supporting Information) Larger value of  $N$  is conducive to the electrical output, and the peak power reaches 2.12 mW under  $80 \text{ M}\Omega$  when  $N = 9$  ( $J = 20 \text{ cm}$ , mass = 1.5 kg, 1 Hz,  $B = D = 6 \text{ cm}$ , Figure 3e). And the DC-TPT can be regarded as a current source when the resistance of the load does not exceed  $2 \text{ M}\Omega$ ,  $5 \text{ M}\Omega$ , and  $100 \text{ M}\Omega$  with  $N = 1, 5$ , and  $9$ , respectively (illustration of Figure 3e). The voltage of a  $10 \mu\text{F}$  electrolytic capacitor can be charged to 13.2 V by the DC-TPT within 30 s (1 Hz,  $J = 20 \text{ cm}$ ,  $N = 9$ , Figure 3f). Moreover, the charging rate increases with the sliding frequency, and it reaches  $2.288 \text{ V } \mu\text{F}^{-1} \text{ min}^{-1}$  at 1.6 Hz ( $N = 5$ , Figure S35, Supporting Information). It is worth noting that not any rectifier is used during charging the capacitors. All the aforementioned results reveal the great potential of our DC-TPT as a DC wearable power source.

#### 2.4. Energy Management Module for the DC-TPT

Although the DC-TPT demonstrates outstanding electrical output capability, the high internal impedance will result in extremely low available energy for powering both energy storage devices and electronics.<sup>[50]</sup> Here, an EMM is designed to solve the above issues, which only contains an input capacitor  $C_i$  and a buck circuit (Figure 4a). The thyristor, a passive electronic switch, is used in the buck circuit to reduce energy loss. When the voltage of  $C_i$  exceeds the breakdown voltage of the Zener diode  $D_1$  (defined as  $V_b$ ), the thyristor will be triggered by a tiny current and turns on until the voltage across it is 0. The detailed working process of EMM is presented in Figure S36 and Note S5 (Supporting Information).  $C_i$  acts as an intermediary between the DC-TPT and buck circuit. The stored energy of  $C_o$  will decrease without  $C_i$  (Figure S37, Supporting Information). A matched capacitor  $C_i$  that is equivalent to the internal resistance of the DC-TPT should be selected to maximize the transferred energy, which is 1.5 nF for the DC-TPT with  $N = 5$  in this work (Figure 4b).

The energy harvested by the DC-TPT can be stored in energy storage devices or drive electronics, the circuit diagrams are

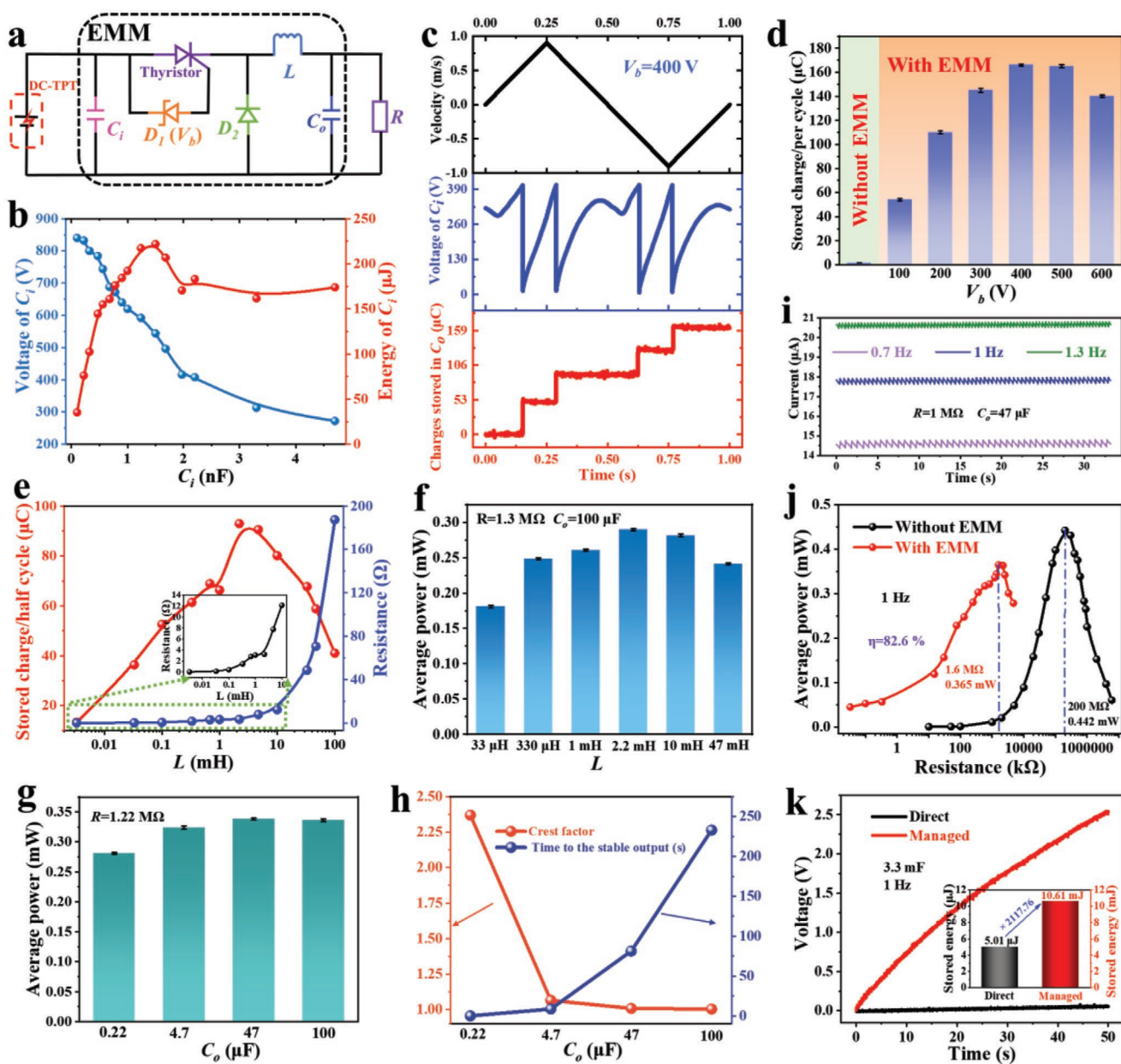


**Figure 4.** Performance of the DC-TPT with EMM. a) Circuit diagram of the DC-TPT powering the external load through EMM. b) The voltage and energy of different capacitors during the half cycle. c) The relationship between the voltage of  $C_i$ , the stored charge of  $C_o$  and the sliding velocity ( $V_b = 400 \text{ V}$ ). d) Stored charge without EMM and under different  $V_b$  values with EMM. e) Variation of the stored charge and f) average power of 1.3 M $\Omega$  load under different inductance values. h) The crest factor, time to the stable output, and g) average power under 1.22 M $\Omega$  load with different  $C_o$ . i) Effect of sliding frequency on output current of the DC-TPT with EMM. j) Average power of DC-TPT under a series of resistances with/without EMM. k) Comparison of charging capacity with/without EMM.

shown in Figure S38 (Supporting Information). Zener diode  $D_1$  can directly control the on and off of the thyristor, of which the voltage value  $V_b$  is crucial. For the energy storage capacity under different  $V_b$  value, the stored charge of a 100  $\mu\text{F}$  capacitor are measured after charging by the DC-TPT with/without EMM in one cycle (Figure 4d). Obviously, all the stored charge values under the management of EMMs with different  $V_b$  values are much higher than that of direct charging capacitor. There are four discharges of  $C_i$  in one cycle when  $V_b = 400 \text{ V}$ , and the stored energy in  $C_i$  is almost completely released into

$C_o$  in each discharge (Figure 4c). Similar results appear under other  $V_b$  values (Figure S39, Supporting Information). The ultrashort stored time of about 1 ms will hardly hinder the next storage stage of the  $C_o$  (Figure S40, Supporting Information). As shown in Figure 4d, the stored charge first increases and then decreases with the increase of the value of  $V_b$  ( $J = 22.5 \text{ cm}$ , 1 Hz,  $B = D = 6 \text{ cm}$ , mass = 2 kg). On the one hand, a higher  $V_b$  value may benefit the energy conversion efficiency from DC-TPT to  $C_o$  (the details are revealed in Note S6, Supporting Information). On the other hand, a higher  $V_b$  value will

increase the maximum voltage before the discharge of  $C_1$  and further exacerbates the leakage of the capacitor. Therefore, there will be an optimal  $V_b$  value. It is demonstrated that the stored charge of  $C_o$  in half cycle increase initially, followed by a decrease with the increasing of the inductance  $L$  value, and it reaches  $92.9 \mu\text{C}$  in half cycle at  $2.2 \text{ mH}$  (Figure 4e). A small  $L$  value will weaken the ability to block the current, which will lead to a large peak current and energy loss. In particular, when there is no inductance, it will become a system of a small capacitor  $C_1$  charges large capacitor  $C_o$  without hindrance, which will resulting in a great heat loss of the parasitic resistance inside the system (Note S7, Supporting Information). However, the internal resistance will increase dramatically as the inductance increases, which will also bring additional losses and further reduce the number of stored charge (Figure S41a, Supporting Information). Similarly,  $2.2 \text{ mH}$  is also the optimized inductance value for driving electronics (Figure 4f), and the increased internal resistance of  $L$  also show a negative effect on the average output power (Figure S41b, Supporting Information). Therefore, to improve the conversion efficiency of EMM,  $L = 2.2 \text{ mH}$  is chosen in the following experiments. The average power of the load ( $1.22 \text{ M}\Omega$ ) does not vary significantly under different  $C_o$  (Figure 4g and Figure S42, Supporting Information). Except for the slight decrease of  $C_o = 0.22 \mu\text{F}$ , which may be due to the leakage of the capacitor (the peak voltage of  $C_o = 0.22 \mu\text{F}$  is  $41.48 \text{ V}$ , while that of the other three capacitors are between  $16.6$  and  $16.8 \text{ V}$ ). Moreover, the crest factor of the current output decreases under high  $C_o$ , while the time to the stable output increases (Figure 4h). The crest factor of the current is calculated by

$$CF = \frac{I_p}{I_{\text{rmf}}} = \frac{I_p}{\sqrt{\frac{1}{T} \int_0^T I^2(t) dt}} \quad (4)$$

where  $I(t)$ ,  $I_p$ ,  $I_{\text{rmf}}$ , and  $T$  are the current at time  $t$ , peak current, root mean square of the current, and period time, respectively. Therefore, small capacitors can be selected when supplying energy to low-power devices to quickly obtain stable output, while large capacitors should be chosen to powering high-power electronic equipment after considering more stable output and reduced leakage of capacitors under high voltage.

Furthermore, higher electrical output can be obtained by increasing the sliding frequency (Figure 4i). And the crest factor of the current output of  $R = 1.22 \text{ M}\Omega$  is only  $1.006$  at  $1.3 \text{ Hz}$  when  $C_o = 47 \mu\text{F}$ . It is worth noting that the crest factor can be further reduced by increasing  $C_o$  value (Figure S42, Supporting Information). High peak power is important for some electronics, such as buzzers and bulbs. Here, EMM can be modified into pulse output mode, the circuit diagram is shown in Figure S43a (Supporting Information). Peak current (calculated by measuring the voltage across the resistor with an ultra-high sampling rate oscilloscope) and peak power can reach  $4.05 \text{ A}$  and  $640.1 \text{ W}$  at  $33 \Omega$ , respectively (Figure S43b,c, Supporting Information). However, the duration of the current is very short due to the rapid discharge of the capacitor (Figure S44, Supporting Information). To discuss the variation of the average power of DC-TPT under different loads with and without EMM,

the average power at  $N = 5$  in Figure 3e is calculated with the following formula

$$P_{\text{ave}} = \frac{1}{T} \int_0^T I^2(t) R dt \quad (5)$$

where  $I(t)$  is the current across the resistor  $R$  at time  $t$ , and  $T$  is the integration time. The average power of DC-TPT with EMM is also calculated (Figure 4j). Since the storage charge of  $C_o$  is similar when  $V_b$  is  $400$  and  $500 \text{ V}$  (Figure 4d), it is necessary to compare their ability when powering load. The current output and average power of the  $150 \text{ k}\Omega$  resistor at  $V_b = 500 \text{ V}$  are slightly higher than those at  $V_b = 400 \text{ V}$  (Figure S45, Supporting Information). Therefore, we chose  $V_b = 500 \text{ V}$  to measure the current of the DC-TPT with EMM and further calculate the average power according to formula (5) under the same experimental conditions as in Figure 3e. The peak current and crest factor both decrease with the increase of resistance, and the current reaches  $174 \text{ mA}$  at  $33 \Omega$  (Figure S46, Supporting Information). The maximum average power of DC-TPT reaches  $0.442 \text{ mW}$  at  $200 \text{ M}\Omega$  without EMM, while the matched resistance drops to  $1.6 \text{ M}\Omega$  with EMM (Figure 4j). And the energy-transfer efficiency is  $82.6\%$ , which is calculated by

$$\eta = \frac{P_{\text{opt-w}}}{P_{\text{opt-wo}}} \quad (6)$$

where  $P_{\text{opt-w}}$  and  $P_{\text{opt-wo}}$  are the maximum average power output with and without EMM, respectively.<sup>[48]</sup> To demonstrate the function of EMM, the current and voltage with and without EMM of a  $30 \text{ k}\Omega$  resistive load are tested (Figure S47, Supporting Information). When the resistor is directly powered by DC-TPT, the peak values of the pulsed current and voltage are only  $6.75 \mu\text{A}$  and  $0.2 \text{ V}$ , respectively (Figure S47a, Supporting Information). However, a stable current of  $68 \mu\text{A}$  and voltage of  $2.15 \text{ V}$  can be obtained after energy management (Figure S47b, Supporting Information). These results show that the EMM can change the low and pulse output to a stable and high output. When DC-TPT directly powers a  $3.3 \text{ mF}$  capacitor, the stored energy is only  $5.01 \mu\text{J}$  within  $50 \text{ s}$ , while it can reach  $10.61 \text{ mJ}$  with  $2117$  times improvement when the EMM is connected (Figure 4k).

## 2.5. Practical Applications

The above results demonstrate that the combination of our high-output DC-TPT and high-efficiency EMM has created a qualitative leap to power low-resistance loads and an increase of thousands of times to charge storage devices. Such surprising consequents make it possible for the naturally wearable DC-TPT to continuously power wearable electronics. Above all, miniaturized EMM is needed to avoid affecting the daily activities of wearer. The electronic components are replaced with SMD (Surface Mounted Devices) type. However, chip inductors ( $2.2 \text{ mH}$ :  $10.24 \Omega$  for CD54 package;  $9.83 \Omega$  for CD75 package) were abandoned due to higher resistance than I inductors ( $2.2 \text{ mH}$ ,  $3.2 \Omega$ ). The experimental results also prove that the EMM with I inductor show a much higher average power than

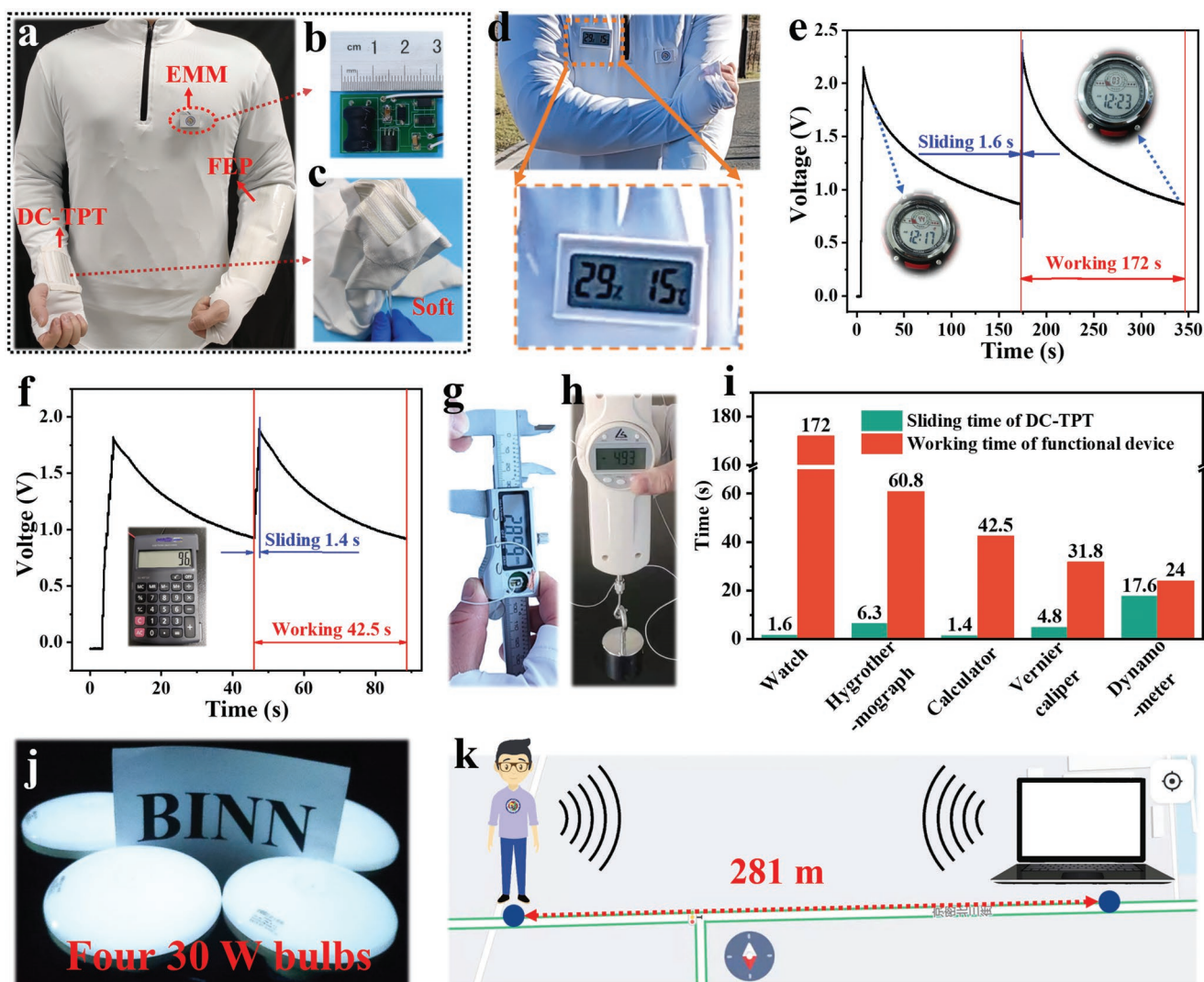


**Figure 5.** Practical applications of the DC-TPT. a) Components of Energy Harvesting Clothes. b) Actual image of EMM and c) the soft DC-TPT. d) Portable hygrothermograph, e) a watch, f) calculator, g) vernier calipers, and h) dynamometers continuously powered by DC-TPT. i) The summary of the sliding time of DC-TPT and the working time of function device. j) Photographs of four 30 W bulbs lit up by DC-TPT. k) Wearable wireless transmission system powered by DC-TPT.

the chip inductor (Figure S48, Supporting Information). Finally, EMM can be prepared on a coin-sized PCB board at a cost of only US\$1.57 (Table S3, Supporting Information). The effect of EMM after miniaturization on PCB board is almost the same as on a breadboard (Figure S49, Supporting Information). The DC-TPT, EMM, and FEP film can be well integrated into our clothes (Figure 5a). The mini EMM (5.8 g) can be encapsulated in a trinket with a logo and worn on the body (Figure 5a,b). Soft DC-TPT ensures energy harvesting clothes retain its original comfort and flexibility (Figure 5c).

Widely used electronic devices, both wearable and non-wearable, such as hygrothermograph (Figure 5d, Movie S1, Supporting Information), watches (Figure 5e, Movie S2, Supporting Information), calculators (Figure 5f, Movie S3, Supporting Information), vernier caliper (Figure 5g, Movie S4, Supporting Information), and dynamometers (Figure 5h, Movie S5, Supporting Information) can be driven continuously

by sliding the on-body DC-TPT manually on our arm. The operating time of the electronic devices is all higher than the sliding time (Figure 5i). Take the watch as an example, just manually sliding the DC-TPT 1.6 s can amazingly drive the watch to work continuously for 172 s, which can fully meet our timing needs (Figure 5e, Movie S2, Supporting Information). In addition, the DC-TPT and EMM worn on the body do not affect our movement (Figure S50, Supporting Information). Moreover, EMM can be varied to pulse output mode. Four 30 W dish bulbs can be lit up by manually sliding the DC-TPT, and the A4 paper with the word “BINN” can be illuminated (Figure 5j and Movie S6, Supporting Information). Wearable DC-TPT can also be used to power wearable portable wireless sensors. We take the transmission of temperature information as an example. The temperature around the tester can be wirelessly transmitted to the monitoring computer 281 m away after sliding the DC-TPT for 2 min (Figure 5k and Movie S7, Supporting Information) Other

information, such as location information and distress signals can also be transmitted over long distances, so as to realize communication with the others and can even save our lives in emergencies when the backup power supply is exhausted. All these demonstrations strongly reveal that DC-TPT and EMM as a wearable power system can meet some urgent needs in our daily life when there is no power supply.

### 3. Conclusions

In summary, we developed an autonomous power textile with a high DC output, full textile, home-preparable DC-TPT and tiny but efficient EMM for sustainable working of mobile and wearable electronics. It is found that PTFE yarn is crucial for the DC-TPT. Its sewing position will seriously affect the output, and even change the working mechanism with a reduced DC electrical output. The electrical output can be scaled up by increasing the number of integrated units, and 5.5  $\mu\text{C}$  charges can be harvested in a sliding area of 120  $\text{cm}^2$  at  $N = 9$  per cycle. There is no noticeable decrease in output of the DC-TPT after agitating 9 h in the washing machine with detergent. The impedance of the DC-TPT is reduced from 200  $\text{M}\Omega$  to 1.6  $\text{M}\Omega$  with an energy conversion efficiency of 82.6% after energy management, which endows the energy-harvesting system with a transferred charge of 95  $\mu\text{C}$  in half cycle and a 2117-fold increase in charging energy storage device. Naturally wearable DC-TPT and miniaturized EMM can be worn on the body as an autonomous power textile to drive wearable electronics. Sliding DC-TPT 1.6 s can keep the watch working for 172 s, and hygrothermograph, calculators, dynamometers, vernier calipers, and wireless sensor can be easily and continuously driven. Moreover, four 30 W bulbs can be lit up to illuminate words on paper in pulse output mode. This work may greatly promote the practical application of on-body biomechanical energy harvester for wearable electronics.

### 4. Experimental Section

**Fabrication of a DC-TPT:** The preparation process of the DC-TPT is very simple and can be prepared at home by nonresearchers. Abrasion-resistant and breathable polyester-cotton textile was chosen as the textile substrate in this work (other kinds of textiles can also work). Above all, Brush the silver paste (quick-drying type with 72 wt% silver) on the surface of a textile that covers the mask (100  $\mu\text{m}$  polyimide) with the shape of the interdigital electrode, followed by drying it in an oven at 100  $^{\circ}\text{C}$  for 10 min. Then, stitch the PTFE yarn with the diameter of 150  $\mu\text{m}$  around the breakdown electrode. Finally, a DC-TPT can be gotten.

**Fabrication of an EMM:**  $V_b = 400$  V was chosen in the miniaturized EMM to discharge more easily after considering the similar electrical output of EMM with  $V_b = 400$  V and 500 V and the irregularity of human motion. The electronic components were soldered on a  $2.9 \times 1.7$   $\text{cm}^2$  PCB according to the circuit diagram in Figure 4a. The miniaturized EMM was then encapsulated in a 3D printed cuboid box ( $3 \times 1.8 \times 1.5$   $\text{cm}^3$ ) with a logo and decorated as a trinket on the clothes.

**Integration of DC-TPT and EMM on the Clothes:** The DC-TPT was sewn on the clothes (it can also be directly prepared on the clothes). The trinket with EMM was stuck to the clothes. The triboelectric layer was attached to the clothes where the DC-TPT can contact easily. Then, the on-body DC-TPT was connected to the EMM and electronic devices in turn through the wires sewn into the clothes to form the autonomous power textile.

**Characterization and Measurements:** The periodic reciprocating motion of the DC-TPT was driven by a linear motor (LinMot E1200), while the short-circuit current and charge transfer were measured by an electrometer (Keithley, model 6514), the high voltage of the DC-TPT was gauged by an oscilloscope (Tektronix, MDO3024) with a high-voltage probe (HVP 3015, 1/1000, 500  $\text{M}\Omega$ ). The breathability of the DC-TPT was tested with an Air Permeability Tester (TQD-G1). Washability test is performed by Haier XPM30-2008, then drying in a 100 $^{\circ}\text{C}$  oven for 15 min. The surface potential on the FEP film was measured by an Isoprobe electrostatic voltmeter (Model 279). The moisture permeability was tested by YG216-I according to GB/T-12704.1-2009.

### Supporting Information

Supporting Information is available from the Wiley Online Library or from the author.

### Acknowledgements

R.C., C.N., and P.C. contributed equally to this work. The authors are grateful for the support received from the National Key R & D Project from the Ministry of Science and Technology (Grant No. 2021YFA1201601), National Natural Science Foundation of China (Grant No. 22109012), Natural Science Foundation of the Beijing Municipality (Grant No. 2212052), and the Fundamental Research Funds for the Central Universities (Grant No. E1E46805). The volunteers took part in the experiments involving wearables following informed consent.

### Conflict of Interest

The authors declare no conflict of interest.

### Data Availability Statement

The data that support the findings of this study are available from the corresponding author upon reasonable request.

### Keywords

air breakdown, direct-current, electronic textiles, energy management, triboelectric nanogenerator

Received: May 4, 2022

Revised: May 30, 2022

Published online:

- [1] F. Ershad, A. Thukral, J. Yue, P. Comeaux, Y. Lu, H. Shim, K. Sim, N-In Kim, Z. Rao, R. Guevara, L. Contreras, F. Pan, Y. Zhang, Y.-S. Guan, P. Yang, Xu Wang, P. Wang, X. Wu, C. Yu, *Nat. Commun.* **2020**, *11*, 3823.
- [2] A. Y. Rwei, W. Lu, C. Wu, K. Human, E. Suen, D. Franklin, M. Fabiani, G. Gratton, Z. Xie, Y. Deng, S. S. Kwak, L. Li, C. Gu, A. Liu, C. M. Rand, T. M. Stewart, Y. Huang, D. E. Weese-Mayer, J. A. Rogers, *Proc. Natl. Acad. Sci. USA* **2020**, *117*, 31674.
- [3] D. Son, J. Kang, O. Vardoulis, Y. Kim, N. Matsuhisa, J. Y. Oh, J. Wf To, J. Mun, T. Katsumata, Y. Liu, A. F. Mcguire, M. Krason, F. Molina-Lopez, J. Ham, U. Kraft, Y. Lee, Y. Yun, J. B.-H. Tok, Z. Bao, *Nat. Nanotechnol.* **2018**, *13*, 1057.

- [4] S. Niu, N. Matsuhisa, L. Beker, J. Li, S. Wang, J. Wang, Y. Jiang, X. Yan, Y. Yun, W. Burnett, A. S. Y. Poon, J. B.-H. Tok, X. Chen, Z. Bao, *Nat. Electron.* **2019**, *2*, 361.
- [5] Z. Zhang, K. Guo, Y. Li, X. Li, G. Guan, H. Li, Y. Luo, F. Zhao, Qi Zhang, B. Wei, Q. Pei, H. Peng, *Nat. Photonics* **2015**, *9*, 233.
- [6] X. Shi, Y. Zuo, P. Zhai, J. Shen, Y. Yang, Z. Gao, M. Liao, J. Wu, J. Wang, X. Xu, Qi Tong, Bo Zhang, B. Wang, X. Sun, L. Zhang, Q. Pei, D. Jin, P. Chen, H. Peng, *Nature* **2021**, *591*, 240.
- [7] K. Dong, Z. Wu, J. Deng, A. C. Wang, H. Zou, C. Chen, D. Hu, B. Gu, B. Sun, Z. L. Wang, *Adv. Mater.* **2018**, *30*, 1804944.
- [8] K. Sim, Z. Rao, Z. Zou, F. Ershad, J. Lei, A. Thukral, J. Chen, Q.-An Huang, J. Xiao, C. Yu, *Sci. Adv.* **2019**, *5*, eaav9653.
- [9] H. Sun, Ye Zhang, J. Zhang, X. Sun, H. Peng, *Nat. Rev. Mater.* **2017**, *2*, 17023.
- [10] G. Chen, Y. Li, M. Bick, J. Chen, *Chem. Rev.* **2020**, *120*, 3668.
- [11] M. Li, H.-W. Lu, S.-W. Wang, R.-P. Li, J.-Y. Chen, W.-S. Chuang, F.-S. Yang, Y.-F. Lin, C.-Y. Chen, Y.-C. Lai, *Nat. Commun.* **2022**, *13*, 938.
- [12] H. Wu, J. Wang, Z. Wu, S. Kang, X. Wei, H. Wang, H. Luo, L. Yang, R. Liao, Z. L. Wang, *Adv. Energy Mater.* **2022**, *12*, 2103654.
- [13] K. Shum, A. Tsatskina, *Nat. Energy* **2016**, *1*, 16188.
- [14] S. Hong, Y. Gu, J. K. Seo, J. Wang, P. Liu, Y. S. Meng, S. Xu, R. Chen, *Sci. Adv.* **2019**, *5*, eaaw0536.
- [15] R. Cheng, K. Dong, L. Liu, C. Ning, P. Chen, X. Peng, Di Liu, Z. L. Wang, *ACS Nano* **2020**, *14*, 15853.
- [16] K. Dong, X. Peng, J. An, A. C. Wang, J. Luo, B. Sun, J. Wang, Z. L. Wang, *Nat. Commun.* **2020**, *11*, 2868.
- [17] Z. L. Wang, *Mater. Today* **2021**, *52*, 348.
- [18] F. Wen, H. Wang, T. He, Q. Shi, Z. Sun, M. Zhu, Z. Zhang, Z. Cao, Y. Dai, T. Zhang, C. Lee, *Nano Energy* **2020**, *67*, 104266.
- [19] C. Zhang, W. Tang, C. Han, F. Fan, Z. L. Wang, *Adv. Mater.* **2014**, *26*, 3580.
- [20] K. Dong, X. Peng, Z. L. Wang, *Adv. Mater.* **2020**, *32*, 1902549.
- [21] W. Weng, P. Chen, S. He, X. Sun, H. Peng, *Angew. Chem., Int. Ed. Engl.* **2016**, *55*, 6140.
- [22] T. He, H. Wang, J. Wang, Xi Tian, F. Wen, Q. Shi, J. S. Ho, C. Lee, *Adv. Sci.* **2019**, *6*, 1901437.
- [23] T. He, X. Guo, C. Lee, *iScience* **2021**, *24*, 101934.
- [24] K. Dong, X. Peng, R. Cheng, Z. L. Wang, *Nanoenergy Adv.* **2022**, *2*, 133.
- [25] K. Dong, J. Deng, W. Ding, A. C. Wang, P. Wang, C. Cheng, Yi-C Wang, L. Jin, B. Gu, B. Sun, Z. L. Wang, *Adv. Energy Mater.* **2018**, *8*, 1801114.
- [26] R. Cheng, K. Dong, P. Chen, C. Ning, X. Peng, Y. Zhang, Di Liu, Z. L. Wang, *Energy Environ. Sci.* **2021**, *14*, 2460.
- [27] K. Dong, X. Peng, R. Cheng, C. Ning, Y. Jiang, Y. Zhang, Z. L. Wang, *Adv. Mater.* **2022**, *34*, 2109355.
- [28] S. Ginnaram, Yi-T Chen, Y.-C. Lai, *Nano Energy* **2022**, *95*, 107035.
- [29] J. Zhu, M. Cho, Y. Li, T. He, J. Ahn, J. Park, T.-L. Ren, C. Lee, I. Park, *Nano Energy* **2021**, *86*, 106035.
- [30] W. He, W. Liu, J. Chen, Z. Wang, Y. Liu, X. Pu, H. Yang, Q. Tang, H. Yang, H. Guo, C. Hu, *Nat. Commun.* **2020**, *11*, 4277.
- [31] P. Chen, J. An, S. Shu, R. Cheng, J. Nie, T. Jiang, Z. L. Wang, *Adv. Energy Mater.* **2021**, *11*, 2003066.
- [32] X. Peng, K. Dong, Y. Zhang, L. Wang, C. Wei, T. Lv, Z. L. Wang, Z. Wu, *Adv. Funct. Mater.* **2022**, *32*, 2112241.
- [33] T. He, C. Lee, *IEEE Open J. Circuits Syst.* **2021**, *2*, 702.
- [34] J. Wang, Y. Li, Z. Xie, Y. Xu, J. Zhou, T. Cheng, H. Zhao, Z. L. Wang, *Adv. Energy Mater.* **2020**, *10*, 1904227.
- [35] P. Chen, J. An, R. Cheng, S. Shu, A. Berbille, T. Jiang, Z. L. Wang, *Energy Environ. Sci.* **2021**, *14*, 4523.
- [36] C. Zhang, T. Zhou, W. Tang, C. Han, L. Zhang, Z. L. Wang, *Adv. Energy Mater.* **2014**, *4*, 1301798.
- [37] J. Wang, Z. Wu, L. Pan, R. Gao, B. Zhang, L. Yang, H. Guo, R. Liao, Z. L. Wang, *ACS Nano* **2019**, *13*, 2587.
- [38] M. Zheng, S. Lin, L. Xu, L. Zhu, Z. L. Wang, *Adv. Mater.* **2020**, *32*, 2000928.
- [39] J. Meng, Zi H Guo, C. Pan, L. Wang, C. Chang, L. Li, X. Pu, Z. L. Wang, *ACS Energy Lett.* **2021**, *6*, 2442.
- [40] Di Liu, X. Yin, H. Guo, L. Zhou, X. Li, C. Zhang, J. Wang, Z. L. Wang, *Sci. Adv.* **2019**, *5*, eaav6437.
- [41] C. Chen, H. Guo, L. Chen, Yi-C Wang, X. Pu, W. Yu, F. Wang, Z. Du, Z. L. Wang, *ACS Nano* **2020**, *14*, 4585.
- [42] H.-J. Yoon, M. Kang, W. Seung, S. S. Kwak, J. Kim, H. T. Kim, S.-W. Kim, *Adv. Energy Mater.* **2020**, *10*, 2000730.
- [43] Z. Zhao, Y. Dai, Di Liu, L. Zhou, S. Li, Z. L. Wang, J. Wang, *Nat. Commun.* **2020**, *11*, 6186.
- [44] Z. Zhao, L. Zhou, S. Li, Di Liu, Y. Li, Y. Gao, Y. Liu, Y. Dai, J. Wang, Z. L. Wang, *Nat. Commun.* **2021**, *12*, 4686.
- [45] C. Wu, A. C. Wang, W. Ding, H. Guo, Z. L. Wang, *Adv. Energy Mater.* **2019**, *9*, 1802906.
- [46] Z. Wang, W. Liu, J. Hu, W. He, H. Yang, C. Ling, Yi Xi, X. Wang, A. Liu, C. Hu, *Nano Energy* **2020**, *69*, 104452.
- [47] D. Bhatia, J. Lee, H. J. Hwang, J. M. Baik, S. Kim, D. Choi, *Adv. Energy Mater.* **2018**, *8*, 1702667.
- [48] Z. Wang, W. Liu, W. He, H. Guo, Li Long, Yi Xi, X. Wang, A. Liu, C. Hu, *Joule* **2021**, *5*, 441.
- [49] W. Tang, T. Zhou, C. Zhang, F. Ru Fan, C. Bao Han, Z. Lin Wang, *Nanotechnology* **2014**, *25*, 225402.
- [50] W. Liu, Z. Wang, G. Wang, Q. Zeng, W. He, L. Liu, X. Wang, Yi Xi, H. Guo, C. Hu, Z. L. Wang, *Nat. Commun.* **2020**, *11*, 1883.
- [51] Z. Cao, S. Wang, M. Bi, Z. Wu, X. Ye, *Nano Energy* **2019**, *66*, 104202.
- [52] H. Zhang, F. Marty, X. Xia, Y. Zi, T. Bourouina, D. Galayko, P. Basset, *Nat. Commun.* **2020**, *11*, 3221.
- [53] F. Xi, Y. Pang, W. Li, T. Jiang, L. Zhang, T. Guo, G. Liu, C. Zhang, Z. L. Wang, *Nano Energy* **2017**, *37*, 168.
- [54] W. Harmon, D. Bamgboje, H. Guo, T. Hu, Z. L. Wang, *Nano Energy* **2020**, *71*, 104642.
- [55] Z. L. Wang, A. C. Wang, *Mater. Today* **2019**, *30*, 34.
- [56] Z. L. Wang, *Rep. Prog. Phys.* **2021**, *84*, 096502.
- [57] C. Zhang, L. Zhou, P. Cheng, X. Yin, Di Liu, X. Li, H. Guo, Z. L. Wang, J. Wang, *Appl. Mater. Today* **2020**, *18*, 100496.
- [58] Yu S Zhou, Y. Liu, G. Zhu, Z.-H. Lin, C. Pan, Q. Jing, Z. L. Wang, *Nano Lett.* **2013**, *13*, 2771.
- [59] Yu S Zhou, S. Li, S. Niu, Z. L. Wang, *Nano Res.* **2016**, *9*, 3705.